Check for updates

Two-Dimensional Silicene–Stanene Heterostructures by Epitaxy

Daya Sagar Dhungana, Carlo Grazianetti,* Christian Martella, Simona Achilli, Guido Fratesi,* and Alessandro Molle*

The synthesis of new Xenes and their potential applications prototypes have achieved significant milestones so far. However, to date the realization of Xene heterostructures in analogy with the well known van der Waals heterostructures remains an unresolved issue. Here, a Xene heterostructure concept based on the epitaxial combination of silicene and stanene on Ag(111) is introduced, and how one Xene layer enables another Xene layer of a different nature to grow on top is demonstrated. Single-phase (4×4) silicene is synthesized using stanene as a template, and stanene is grown on top of silicene on the other way around. In both heterostructures, in situ and ex situ probes confirm layer-by-layer growth without intercalations and intermixing. Modeling via density functional theory shows that the atomic layers in the heterostructures are strongly interacting, and hexagonal symmetry conservation in each individual layer is sequence selective. The results provide a substantial step toward currently missing Xene heterostructures and may inspire new paths for atomic-scale materials engineering.

The advent of Xenes has recently reshaped the research frontiers of the emerging 2D materials[1,2] by expanding the available options beyond well-known members like graphene and transition metal dichalcogenides (TMDCs) and, hence, the inherent recombination in complex and mixed heterostructures.[3] Silicene[4,5] has paved the way to the currently increasing number of successive Xenes on the stage of potential applications to be derived from refs. [6–11].

Piling up 2D crystal layers in so-called van der Waals (vdW) heterostructures was a key cross-point in the evolution of 2D

materials toward the exploitation of a richer spectrum of physical properties arising from the sequential coupling in the stack kept together through vdW interactions at variance with the epitaxy of conventional heterostructures.[12–15] This was the case of graphene layer and hBN-based tunneling field effect transistors and plasmonics devices, photodiodes constructed with graphene and TMDCs layers, Li-ion battery built with MoS_2 and graphene layers, and many more as elaborated in refs. [12–15]. Making Xene heterostructures would bring substantial benefits in the framework of the science and technology of emerging 2D materials, for example, enabling the combination of different Xenes toward functionally coupled heterojunctions, facilitating the individual Xene layer disassembly from its native substrate, and ultimately paving the way to Xene-based superlattices (namely multiple elementary atomically thin layers stacked together). However, while Xenes are individually isolated with sophisticated epitaxial methods on compliant substrates,[1,6,7] the synthesis of Xene heterostructures by design is quite puzzling, whereas some hints of homostructures have been already reported.[16] One work in this respect reported on the inability of germanium to grow as germanene on a silicene template.[17] This was a clear warning on the requested matching when arranging a Xene on top of another one of different chemical species in order to avoid 3D growth like clustering or amorphization. Other approaches to the issue include the vertical and lateral interfacing of silicene with graphene,[18–20] differential segregation from substrate,[21] and topotactic intercalation.[22]

In the present work, we show how two well-established Xene configurations, that is, silicene-on-silver[4] and stanene-on-silver,[23] may serve as suitable templates for the epitaxy of the reciprocal Xene single-layer on top. More specifically, based on an epitaxial method aiming at the Xene production on the macro-scale, we demonstrate the scalable production of silicene–stanene heterostructures by design starting from a (111)-terminated silver substrate by means of carefully tailored process parameters, and quick and reliable diagnostics, therein enabling a more facile scheme to isolate a single Xene layer (by sacrificing the other one in the heterostructure) or the whole heterostructure (by taking benefit from the competing Si-Sn interaction with respect to that with the Ag substrate) by means of already developed process protocols.[24] The initial configuration

Dr. D. Dhungana, Dr. C. Grazianetti, Dr. C. Martella, Dr. A. Molle
CNR-IMM Agrate Brianza Unit
via C. Olivetti 2, Agrate Brianza I-20864, Italy
E-mail: carlo.grazianetti@mdm.imm.cnr.it;
alessandro.molle@mdm.imm.cnr.it
Dr. S. Achilli, Prof. G. Fratesi
ETSF and Physics Department "Aldo Pontremoli"
University of Milan
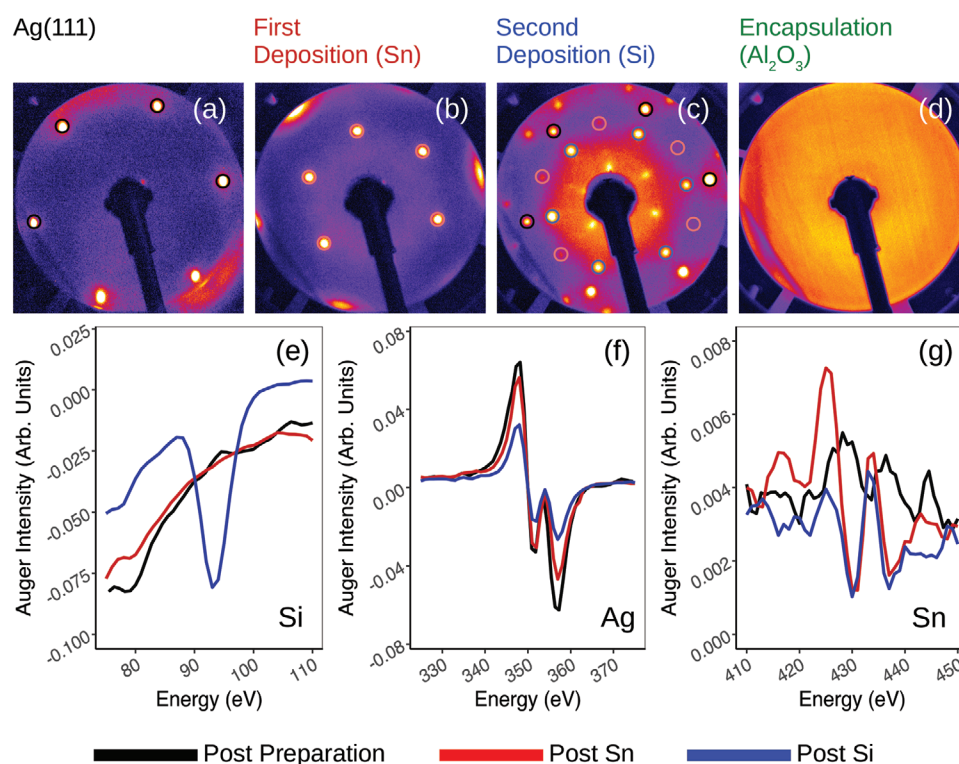via Celoria 16, Milano I-20133, Italy
E-mail: guido.fratesi@unimi.it

Figure 1. Heterostructure type-I: Silicene on top of Sn:$\sqrt{3} \times \sqrt{3}$ R30°/Ag(111). a–d) LEED patterns obtained: post preparation at incident energy (E_i) = 49 eV (a), after Sn deposition at E_i = 33 eV (b), after Si deposition at E_i = 52 eV (c), and after non-reactive Al_2O_3 encapsulation at E_i = 49 eV (d). Sharp hexagonal Ag:1 × 1 LEED patterns (black circles) following sputtering and subsequent annealing (a). First order Sn:$\sqrt{3} \times \sqrt{3}$ R30° patterns (red circles) observed after 1.33 monolayers Sn deposition at 225 °C (b). Silicene: 4 × 4 LEED spots (blue circles) acquired after depositing one monolayer Si on top of Sn (b) at 225 °C (c) and capping layer (amorphous and non-reactive Al_2O_3) in order to facilitate ex situ analysis (d). e–g) Auger spectra: (black) post-preparation curve corresponding to the as-prepared Ag(111) surface (a), (red) post Sn deposition curve corresponding to the as-grown stanene layer (b), and (blue) post Si deposition curve corresponding to surface (c). (e), (f), and (g), respectively, feature the region of interest for Si (E_i = 92 eV), Ag (E_i = 354 eV), and Sn (E_i = 430 and 437 eV). Figures S1 and S2, Supporting Information, report LEED patterns acquired at different E_i, respectively, for (b) and (c).

of both silicene-on-silver and stanene-on-silver replicate previously reported standards[4,23] while the second layer is identified by in situ probing of the diffraction pattern by means of low energy electron diffraction (LEED), and by in situ and ex situ spectroscopies. We show the sequential order in the layer stacking dramatically affects the details of the layer atomic symmetry. Hence, making silicene–stanene heterostructures aims at opening the door to a completely unexplored field of Xene heterostructures where different Xene combinations are made by design and may take benefit from the synergy of the two constituting components (e.g., topological effect and electronic band structure engineering).

In this framework, we first report on the type-I heterostructure (top-to-bottom: Al_2O_3–Si–Sn–Ag(111)/mica) in **Figure 1** where epitaxial 1.33 monolayers-thick Sn and amorphous Al_2O_3 capping layer[25] ($\approx$5 nm) sandwich a Si monolayer in between. The LEED patterns acquired from freshly prepared Ag(111) (Figure 1a) and post Sn deposition, that is, after 1.33 Sn monolayers at 225 °C, (Figure 1b and Figure S1, Supporting Information) show that Sn grows by assuming a $\sqrt{3} \times \sqrt{3}$ R30° reconstruction on the pristine (111)-terminated Ag surface. This scenario is consistent with the emergence of a highly planar stanene observed by Yuhara et al.[23] as a result of the Sn grown on a preformed Ag_2Sn template (Yuhara-like stanene in the following). A similar arrangement has been recently observed

by Sn epitaxy on Au(111) with interfacial engineering of the released strain.[26,27] On top of this so-reconstructed stanene, we observe Si to grow with a 4 × 4-reconstructed silicene single-phase fashion (Figure 1c and Figure S2, Supporting Information; Figure S5, Supporting Information, for silicene growths at different temperatures). The latter evidence strikingly deviates from silicene directly grown on top of Ag(111) where the same 4 × 4 reconstruction mixes up with $\sqrt{13} \times \sqrt{13}$ phases (and other minority phases),[28–30] and claims for the realization of a single-phase silicene monolayer. The corresponding in situ Auger spectra (Figure 1e–g) first confirm the attenuation of the Ag peak at E_i = 354 eV in Figure 1f after piling up sequential layers from the initial Ag(111) surface (Figure 1a; black curve in Figure 1f) up to the $\sqrt{3} \times \sqrt{3}$ R30°-reconstructed stanene (Figure 1b; red curve in Figure 1f) and finally to a 4 × 4 silicene superstructure (Figure 1c; blue curve in Figure 1f). The same behavior holds on for the Sn peaks (Figure 1g at E_i = 430 and 437 eV) when Si comes on top (Figure 1c; blue curve in Figure 1g) thus making evidence of a layer-by-layer growth mechanism of the atomic single layers.

Now we turn the attention toward the type-II heterostructure (Al_2O_3–Sn–Si–Ag(111)/mica from top to bottom), in **Figure 2**, where the Xenes sequence is reversed with respect to the type-I heterostructure (Figure 1), while the growth parameters for each single layer are left unchanged. First, mixed
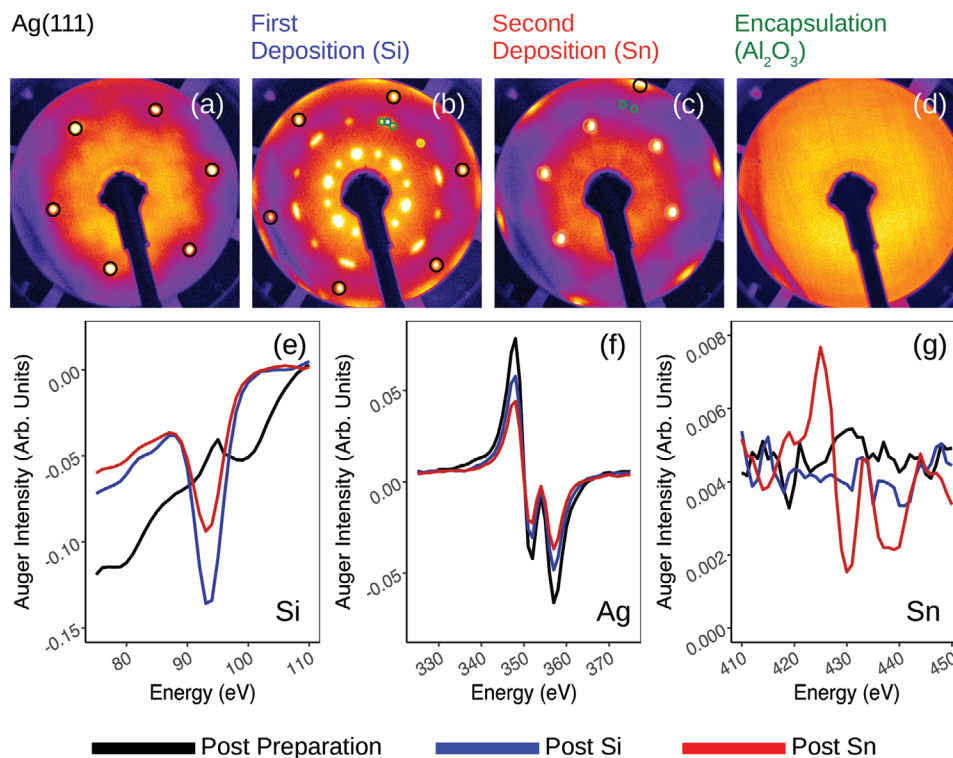
**ADVANCED
SCIENCE NEWS**
www.advancedsciencenews.com

**ADVANCED
FUNCTIONAL
MATERIALS**
www.afm-journal.de

Figure 2. Heterostructure type-II: Sn:√3 × √3 R30° on top of mixed Silicene/Ag(111). a–d) LEED patterns obtained: post preparation at incident energy (E_i) = 49 eV (a), after Si deposition at E_i = 56 eV (b), after Sn deposition at E_i = 33 eV (c), and after non-reactive Al_2O_3 encapsulation at E_i = 49 eV (d). Ag:1 × 1 LEED patterns (black circles) following sputtering and subsequent annealing (a). Mixed silicene phases (represented once): √13 × √13 R13.9° type I (green circle), √13 × √13 R13.9° type II (yellow circle), and 4 × 4 (blue circle) observed following the one monolayer Si deposition at 225 °C (b). √3 × √3 R30° LEED spots (red circles) acquired by depositing 1.33 monolayers Sn on top of silicene (b) at 225 °C (c). Capping layer (amorphous and non-reactive Al_2O_3) in order to facilitate ex situ analysis (d). e–g) Auger spectra: (black) post-preparation curve corresponding to a freshly prepared Ag(111) surface (a), (blue) post Si deposition curve corresponding to the as-grown silicene layer (b), and (red) post Sn deposition curve corresponding to the as-grown stanene layer (c). Similar to Figure 1e–g, (e), (f), and (g) feature the region of interest, respectively, Si (E_i = 92 eV), Ag (E_i = 354 eV), and Sn (E_i = 430 and 437 eV). Figures S3 and S4, Supporting Information, present LEED patterns acquired at different E_i, respectively, for (b) and (c).

silicene phases[28–30] (gathering 4 × 4, √13 × √13 R13.9° phases altogether) are clearly visible on top of Ag(111) from the LEED pattern in Figure 2b (and Figure S3, Supporting Information), as expected after silicene epitaxy.[28–30] Next, following Sn deposition on top of the same mixed silicene surface, the characteristic √3 × √3 R30° structure can be deduced from the LEED pattern (Figure 2c and Figure S4, Supporting Information; and Figures S6 and S7, Supporting Information, for Sn depositions on top of various silicene surfaces) that is apparently similar to that observed in the type-I heterostructure (for Sn being under Si) and again consistent with the Yuhara-like stanene.[23] Along with these characteristics are traces of silicene lattice underneath in the LEED pattern. Similarly, the in situ Auger spectra (Figure 2e–g) also follow the same trend of the previously scrutinized type-I heterostructure. In detail, the attenuation of Ag peak at E_i = 354 eV in Figure 2f, from black-to-blue and blue-to-red, consecutively with two depositions rounds as well as the Si peak at E_i = 92 eV in Figure 1e from blue-to-red post Sn deposition (Figure 2c) again suggest a layer-by-layer growth in this heterostructure with no evidence of intercalations or interlayer or intrasubstrate diffusions.[31] Scalability of the two heterostructures is demonstrated by means of in situ LEED surface mapping (Figure S8, Supporting Information) throughout the whole sample area (4 × 3 mm²) therein displaying no variation

as a function of the position. The layer-by-layer character of the growth sequence is consistent with the behavior of the Auger peak intensity with each process stage for both heterostructures (see Table S1, Supporting Information). In addition, sequential LEED monitoring stage allows us to rule out the significant emergence of 3D structures after second Xene growth as no diffraction spot splitting, deformation, or intensity spread can be observed.

We stabilized the heterostructures with a non-reactive Al_2O_3 encapsulation (see ref. [25] for more details), protecting them from degradation out of the growth environment and hence enabling ex situ characterization via Raman spectroscopy (**Figure 3**a,b) and X-ray photoelectron spectroscopy (XPS) (Figure 3c–f). First, both Raman spectra, blue (Figure 3a) and red (Figure 3b), respectively, for heterostructure type-I and type-II, are characterized by an intense first-order silicene peak and an asymmetric and broad shoulder at lower frequency. The main silicene peaks are located at Raman shifts in the range 518–519 cm⁻¹, that are slightly larger than that reported for encapsulated silicene single-layer on silver obtained in the same growth condition.[32–34] This frequency upshift stems from the specific details of the Sn–Si interaction, which, based on the density functional theory (DFT) calculations reported in Figure S11a, Supporting Information, can be related to several
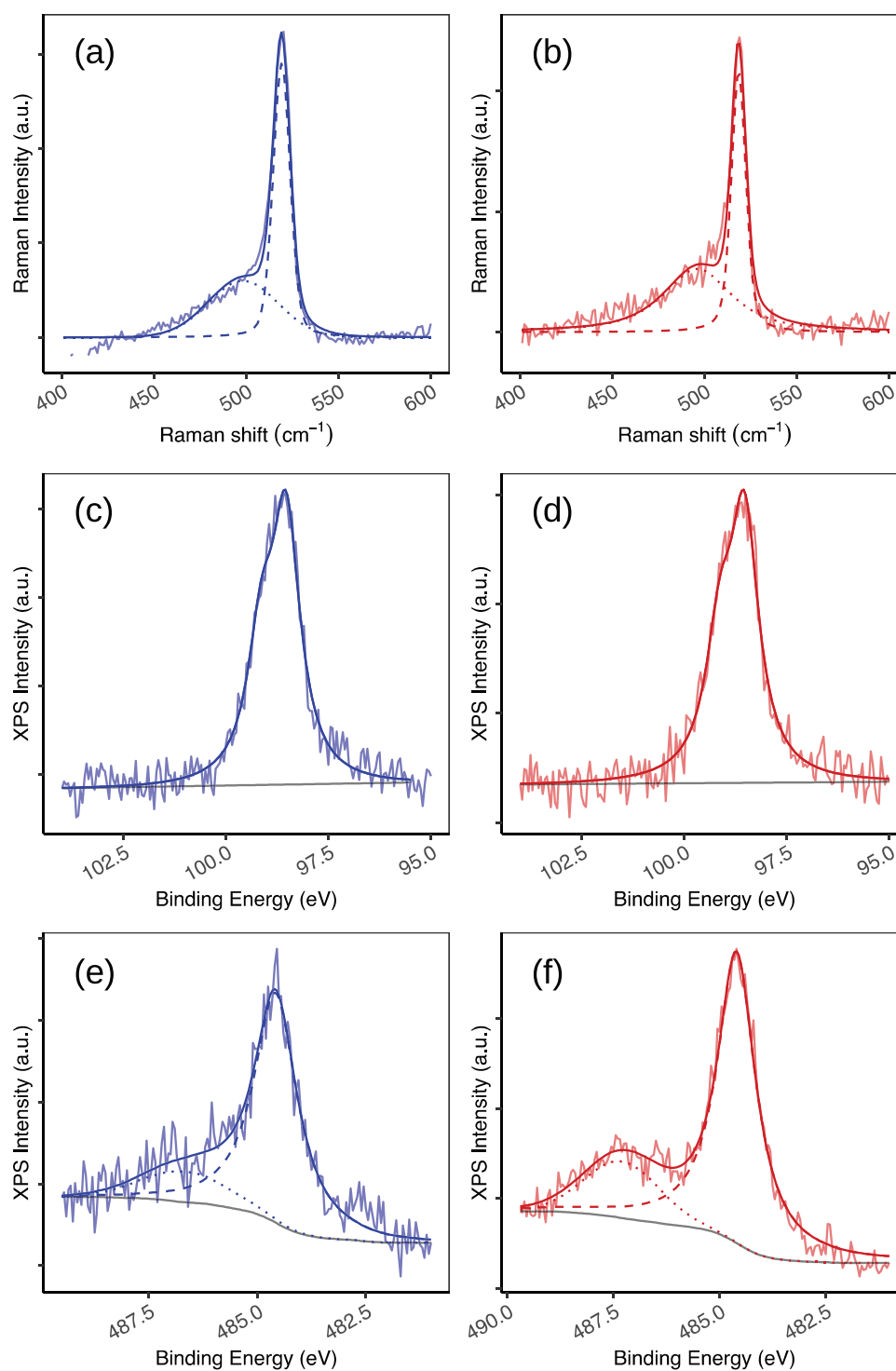
Figure 3. Ex situ characterizations: a,b) Micro-Raman spectra of heterostructure type-I (blue) (a) and heterostructure type-II (red) (b). In both the cases, the faint curve represents raw data; while solid, dashed, and dotted curves are fits obtained using Lorentzian–Gaussian components. For both, the spectra are characterized by an intense first-order silicene peak centered ≈518–519 cm^{-1} and an asymmetric and broad shoulder at lower frequency. c–f) XPS core levels of type-I and type-II Xenes heterostructures. Si 2p core level where light blue (type-I heterostructure) (c) and light red (type-II heterostructure) (d) are raw data while dark blue and red are full fit for heterostructure type-I and II, respectively. Sn $3d_{5/2}$ core level where dark blue (type-I heterostructure) (e) and red curve (type-II heterostructure) (f) are full fit respective for raw data in light blue and light red. Dashed and dotted lines curves are metallic and oxidized components, respectively, in both the cases. For both heterostructures, Si 2p and Sn $3d_{5/2}$ core level are, respectively, centered at 98.53 and 486 eV. See Figure S9, Supporting Information, for Ag $3d_{5/2}$ core levels.

physical effects including charge transfer, modifications of the projected density of states, and of the lattice coordinates (buckling). Furthermore, the Raman evidence per se confirms the silicene layer is robust against Sn incorporation in the heterostructure either above (by deposition) or below (as template). On the other hand, Raman investigation of both heterostructures does not show characteristic spectral signatures of Sn, even when probed with diverse excitation wavelengths. This fact is common to other stanene configurations[26] and is likely due to an intrinsic metallic character in the so-structured Yuhara-like stanene.[23] Consistent with the in situ LEED surface mapping, large-area uniformity of the encapsulated heterostructures is validated by μ-Raman spectroscopy monitoring as a function of the position on the sample surface.

In order to get through the chemical stability of the so-grown Xene heterostructures, XPS analysis was carried out in a second ultrahigh vacuum (UHV) system after air exposure of the encapsulated Xene heterostructures as reported in Figure 3c–f. Interestingly, the binding energy of Si 2p is not affected by the heterostructure type as they both show a single narrow component at binding energy (E_b) of 98.53 eV (Figures 3c [blue] and 3d [red] lines for type-I and type-II heterostructure, respectively) in good agreement with previous studies.[35–37] Conversely, in both heterostructures considered, Sn is more prone to partially undergo oxidation as results from the deconvolution of the Sn $3d_{5/2}$ line in a narrow elemental bonding component at lower E_b and a broader oxide-related component at higher E_b that is consistent with the formation of minor SnO_2 content[38] (Figures 3e [blue] and 3f [red] lines for type-I and type-II heterostructure, respectively, and Figure S9, Supporting Information, about the Ag $3d_{5/2}$ line). It can be noticed that the oxide component in the Sn $3d_{5/2}$ line is more intense in the type-II heterostructure than in the type-I one; this fact being likely related to the preferential oxidation of Sn closer to the capping layer as in type-II heterostructure. On the other hand, the elemental Sn component is placed at $E_b = 484.58$ eV (484.6) for type-I (type-II) heterostructure in substantial agreement with the binding energy positioning reported for elemental Sn.[39] The binding energies of the Si 2p and Sn $3d_{5/2}$ core-level photoemission lines therefore rule out the chemical intermixing or alloying between the Xene layers.

For a deeper insight into the structural stability and electronic structure of the experimentally reported Xene heterostructures, we performed DFT calculations of the two cases in point, taking the experimental data as inputs for the starting models (see Experimental Section) and then performing structural optimization. In the type-I heterostructure (**Figure 4**a), Sn is modeled as a pristine honeycomb stanene lattice supported by an Ag_2Sn template as computed by Yuhara et al.[23] Overlapping a silicene layer bends the pristine stanene into a distorted lattice then breaking the original honeycomb structure on the substrate while retaining the original $\sqrt{3} \times \sqrt{3}$ R30° symmetry. The destroyed structural symmetry stems from the local Si–Sn interaction but the Sn layer keeps a moderate buckling (0.52 Å at most) and does not intermix with the upper Si layer. Despite the symmetry breaking in the pristine stanene, silicene turns out to preserve its hexagonal structure. This outcome allows us to redefine the atomistic details of the type-I heterostructure as a stacking of an originally grown Yuhara-like stanene ending up, after deposition of a silicene layer on top, in a distorted structure of an atomically thin (non-stanene) Sn nanosheet, possibly lacking a specific order, on top of an Ag_2Sn substrate layer
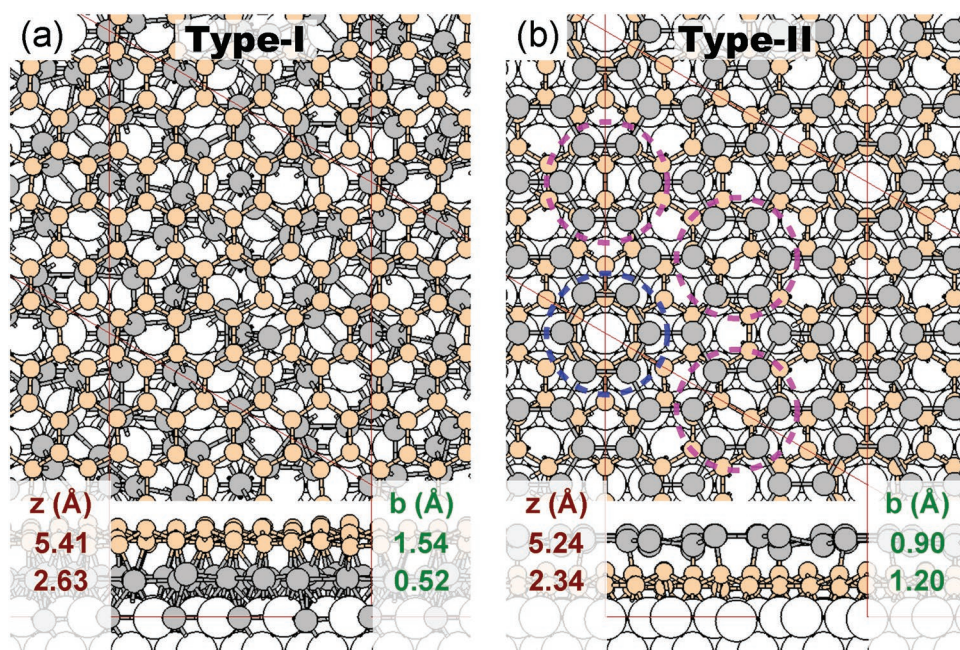

Figure 4. Theoretical models resulting from DFT structural optimizations: a) type-I heterostructure and b) type-II heterostructure. In all cases a top- and a side-view are shown with the larger white spheres representing Ag atoms, medium-sized gray Sn ones, and smaller orange Si ones. The thin red line marks our $4\sqrt{3} \times 4\sqrt{3}$ R30° supercell. The numbers in red (on the left of each plot) indicate the average height z of the Si and Sn layers over the bulk-truncated Ag surface, and those in green (right) the corresponding buckling ($b = z_{max} - z_{min}$). Magenta/blue circles in (b) mark Sn hexagons at higher/lower height over the surface.

but still retaining an (overall) $\sqrt{3} \times \sqrt{3}$ R30° symmetry. Type-I heterostructure then recasts as an alternation of atomically thin sheets where the Sn layer loses its original honeycomb structure and serves as a template for the epitaxy of a single-phase 4×4 silicene otherwise not achievable in (111)-terminated metal surfaces.

On the other hand, an energetically stable stanene-on-silicene configuration takes place for a type-II heterostructure (Figure 4b) starting from 4×4 silicene on Ag(111) and over-imposing a $\sqrt{3} \times \sqrt{3}$ R30° stanene sheet. This condition allows silicene to host a stable $\sqrt{3} \times \sqrt{3}$ R30° stanene structure which only shows small displacements from the ideal honeycomb lattice consistent with the experimentally observed LEED pattern (Figure 2). In this picture, one can observe Sn hexagons at different heights over the surface, bridged by Sn atoms significantly closer to the surface (see the Figure S10, Supporting Information). Inspection of the electronic properties of both heterostructures (reported in the Figure S11, Supporting Information) leads us to conclude that the interface components are strongly hybridized, as already found for the silicene–silver interface as far as all layers exhibit a high electronic density of states around the Fermi energy[40–44] and clear signatures of the electronic structure of free-standing layers are only present at energies below the Ag d band. Hybridization with substrate states in adsorbed silicene could be reduced by growth on non-metallic substrates,[45,46] or by intercalation of O atoms.[37] Mülliken charges show that in both interfaces the sandwiched layer becomes negatively charged (type-I, Sn: 0.02e/atom; type-II, Si: 0.06e/atom), whereas the upper layer is almost neutral (type-I, Si: –0.01e/atom; type-II, Sn: 0.00e/atom).

The DFT modeling gives us a direction to understand to what extent Xenes may be exchanged in the sequence of a heterostructure with or without keeping their individual atomic lattice. This scenario is reconciled with the experimental one with the following conditions: a) the Si growth results in a silicene lattice irrespectively of the given epitaxial template, namely silicene sets in as a top or bottom layer when grown on Sn (type-I heterostructure) or Ag (type-II heterostructure), respectively; b) the Sn may result in a stanene lattice only when deposited onto a silicene template on the bottom (type-II heterostructure), whereas the honeycomb symmetry is broken and a distorted layer takes place whenever stanene buffers silicene from Ag (type-I heterostructure). Although the so-grown heterostructures exhibit exchangeable atomically thin and chemically defined layers of Si and Sn with no apparent chemical or physical recombination, the (buckled) honeycomb character of silicene and stanene cannot commute with the growth sequence and only the Sn–Si–Ag directional growth (resulting in the so-called type-II heterostructure) identifies a true Xene heterostructure fashion. The epitaxy on an Ag(111)/mica substrate and the Al_2O_3 encapsulation enable the Xene heterostructures to be disassembled from the pristine substrate for transfer to secondary substrate thus allowing for their device or functional applications.[24]

In summary, we unveiled a novel heterostructure growth regime where the Sn and Si growth order is exchangeable. Based on DFT calculations, only the top-to-bottom sequence Sn–Si–Ag (type-II heterostructure) can preserve the emergence and stability of buckled honeycomb layers (pure Xene heterostructure),

namely stanene and silicene, whereas the reversed order affects the stanene symmetry though keeping an atomic Sn sheet in between the Ag substrate and the top silicene (pseudo-Xene heterostructure). This new concept of Xene heterostructures can be interesting to probe quantum physics in the Xene regime and to expand the technology potential of the Xenes upon recombination in heterostructures by design. Epitaxial Xenes like germanene,[47] borophene,[48,49] antimonene,[50] phosphorene,[51] and tellurene[52] (and others yet to come) may fit the purpose thus expanding the number of possible Xene heterostructures onward. Our in situ LEED and Auger analysis indicate a new crystalline phase occurs in both cases, and the growth is layer-by-layer without any signs of intercalation or chemical alloying. We also showed that it is possible to realize single phase silicene 4×4 by growing on top of Sn:$\sqrt{3} \times \sqrt{3}$ R30° surface which can be easily grown on top of the Ag(111) surface. We further believe this single phase 4×4 silicene addresses one of the critical bottlenecks (along with the Ag layer removal) in view of silicene transistor fabrication. Having addressed the large-scale epitaxy of silicene–stanene heterostructures, the disclosed scenario provides an open room for atomically resolved investigations to elucidate would the details of the second Xene layer locally. These outcomes thus extend the so called Lego-like approach originally deemed for assembling 2D vdW crystals to the Xenes family thus opening new routes to artificial materials fabrication on-demand.

Experimental Section

Synthesis and In Situ Characterization: The epitaxy of Xenes heterostructures were carried out at CNR-IMM Unit of Agrate Brianza using Scienta Omicron Solid-Source(SS) Lab10 MBE system that was equipped with in situ LEED and Auger electron spectroscopy (AES), in addition to in situ Ar⁺ ion sputtering in the preparation chamber, that was integrated to the growth chamber. The base pressure of both the chambers was $<5 \times 10^{-10}$ mbar. LEED and AES acquisitions were performed by means of a Scienta Omicron GmbH LEED 600 apparatus working with a LaB_6 filament and with a nominal beam spot size of 500 μm during LEED operation. The synthesis part, where each step was accompanied with in situ LEED and Auger analysis, comprises the three major steps: i) preparation of commercial 300 nm-thick (epitaxial) Ag(111)/mica substrate with several cycles of Ar⁺ sputtering (1 kV/10 mA ion source) at room temperature followed with subsequent high temperature annealing (550 °C for 30 min); ii) Si and Sn deposition, respecting the sequence on heterostructure type, respectively, at 0.03 and 0.015 monolayers per minute at 225 °C; and iii) a non-reactive amorphous Al_2O_3 capping as described elsewhere.[25]

Ex Situ Characterization: Following encapsulation, ex situ Raman spectroscopy was performed in back-scattering configuration using a Renishaw InVia spectrometer equipped with the 514 nm (2.41 eV) line of a solid state laser. The incident laser power was kept below 1 mW to avoid sample damages.

XPS was performed on air exposed samples in a separated UHV system. The chemical status of the Xene heterostructures was monitored by means of non-monochromatized XPS source ($h\nu$ = 1253.6 eV). Bulk sensitive measurements were performed at take-off angle of 80° between sample surface and hemispherical electron analyzer in order to bypass the capping layer.

Density Functional Theory Simulations: The authors performed ab initio simulations within DFT exploiting the SIESTA code.[53,54] Norm-conserving pseudopotentials from the software library libPSML[55] and the Perdew–Burke–Ernzerhof[56] exchange and correlation functional were used. Dispersion forces were added by the Grimme-D2 approach.[57]

**ADVANCED
SCIENCE NEWS**

www.advancedsciencenews.com

**ADVANCED
FUNCTIONAL
MATERIALS**

www.afm-journal.de

The Ag(111) support was modeled by a three-layer thick slab, with Sn and Si adsorbed on one side, for the structure relaxation calculation, while the thickness was increased to six layers for the analysis of the electronic properties. The authors started from previously established models for the adsorption of individual Sn and Si as honeycomb stanene on $SnAg_2$ surface alloy on Ag(111)-$(\sqrt{3} \times \sqrt{3})$[23] and silicene-$(3 \times 3)$ on Ag(111)-(4×4).[4] To match the experimentally observed periodicity of the heterostructures with periodic boundary conditions imposed by the simulations and the periodicity of the pristine Xene layers, the authors took a $4\sqrt{3} \times 4\sqrt{3}$ R30° supercell with 230 atoms, noticing that this specific choice followed from the experimental characterization supplanting the theoretical identification of other candidate structures exhibiting a different periodicity. The surface Brillouin zone was sampled by a 2×2 mesh of k-points, increased to 10×10 for the calculation of the density of states (reported in the Figure S11, Supporting Information). The systems had been relaxed until the forces reached the imposed threshold of 0.04 eV Å⁻¹. The results were checked for smaller supercells by comparison with plane-wave calculations performed by the pseudopotential code Quantum ESPRESSO.[58]

Supporting Information

Supporting Information is available from the Wiley Online Library or from the author.

Conflict of Interest

The authors declare no conflict of interest.

Data Availability Statement

The data that support the findings of this study are openly available in Zenodo at https://zenodo.org/record/4462805#.YA7dBC1aafU, doi:10.5281/zenodo.4462805.

[1] A. J. Mannix, B. Kiraly, M. C. Hersam, N. P. Guisinger, *Nat. Rev. Chem.* **2017**, *1*, 0014.

[2] A. Molle, J. Goldberger, M. Houssa, Y. Xu, S. C. Zhang, D. Akinwande, *Nat. Mater.* **2017**, *16*, 163.

[3] A. K. Geim, I. V. Grigorieva, *Nature* **2013**, *499*, 419.

[4] P. Vogt, P. De Padova, C. Quaresima, J. Avila, E. Frantzeskakis, M. C. Asensio, A. Resta, B. Ealet, G. L. Lay, *Phys. Rev. Lett.* **2012**, *108*, 155501.

[5] B. Feng, Z. Ding, S. Meng, Y. Yao, X. He, P. Cheng, L. Chen, K. Wu, *Nano Lett.* **2012**, *12*, 3507.

[6] N. R. Glavin, R. Rao, V. Varshney, E. Bianco, A. Apte, A. Roy, E. Ringe, P. M. Ajayan, *Adv. Mater.* **2020**, *32*, 1904302.

[7] C. Grazianetti, C. Martella, A. Molle, *Phys. Status Solidi RRL* **2020**, *14*, 2070013.

[8] A. Zhao, B. Wang, *APL Mater.* **2020**, *8*, 030701.

[9] T. Wang, H. Wang, Z. Kou, W. Liang, X. Luo, F. Verpoort, Y.-J. Zeng, H. Zhang, *Adv. Funct. Mater.* **2020**, *30*, 2002885.

[10] W. Tao, N. Kong, X. Ji, Y. Zhang, A. Sharma, J. Ouyang, B. Qi, J. Wang, N. Xie, C. Kang, H. Zhang, O. C. Farokhzad, J. S. Kim, *Chem. Soc. Rev.* **2019**, *48*, 2891.

[11] A. K. Tareen, K. Khan, M. Aslam, H. Zhang, X. Liu, *Nanoscale* **2020**, *13*, 510.

[12] K. S. Novoselov, A. Mishchenko, A. Carvalho, A. H. C. Neto, *Science* **2016**, *353*, aac9439.

[13] L. Britnell, R. M. Ribeiro, A. Eckmann, R. Jalil, B. D. Belle, A. Mishchenko, Y. J. Kim, R. V. Gorbachev, T. Georgiou, S. V. Morozov, A. N. Grigorenko, A. K. Geim, C. Casiraghi, A. H. C. Neto, K. S. Novoselov, *Science* **2013**, *340*, 1311.

[14] C. H. Lee, G. H. Lee, A. M. Van Der Zande, W. Chen, Y. Li, M. Han, X. Cui, G. Arefe, C. Nuckolls, T. F. Heinz, J. Guo, J. Hone, P. Kim, *Nat. Nanotechnol.* **2014**, *9*, 676.

[15] F. Withers, O. Del Pozo-Zamudio, A. Mishchenko, A. P. Rooney, A. Gholinia, K. Watanabe, T. Taniguchi, S. J. Haigh, A. K. Geim, A. I. Tartakovskii, K. S. Novoselov, *Nat. Mater.* **2015**, *14*, 301.

[16] J. Gou, L. Kong, X. He, Y. L. Huang, J. Sun, S. Meng, K. Wu, L. Chen, A. T. S. Wee, *Sci. Adv.* **2020**, *6*, eaba2773.

[17] D. S. Lin, in *Encyclopedia of Interfacial Chemistry*, (Ed: K. Wandelt), Elsevier, Amsterdam **2018**, pp. 155–161.

[18] B. Kiraly, A. J. Mannix, M. C. Hersam, N. P. Guisinger, *Chem. Mater.* **2015**, *27*, 6085.

[19] G. Li, L. Zhang, W. Xu, J. Pan, S. Song, Y. Zhang, H. Zhou, Y. Wang, L. Bao, Y. Y. Zhang, S. Du, M. Ouyang, S. T. Pantelides, H. J. Gao, *Adv. Mater.* **2018**, *30*, 1804650.

[20] H. Guo, R. Zhang, H. Li, X. Wang, H. Lu, K. Qian, G. Li, L. Huang, X. Lin, Y. Y. Zhang, H. Ding, S. Du, S. T. Pantelides, H. J. Gao, *Nano Lett.* **2020**, *20*, 2674.

[21] T. Ogikubo, H. Shimazu, Y. Fujii, K. Ito, A. Ohta, M. Araidai, M. Kurosawa, G. L. Lay, J. Yuhara, *Adv. Mater. Interfaces* **2020**, *7*, 1902132.

[22] A. M. Tokmachev, D. V. Averyanov, I. A. Karateev, O. E. Parfenov, O. A. Kondratev, A. N. Taldenkov, V. G. Storchak, *Adv. Funct. Mater.* **2017**, *27*, 1606603.

[23] J. Yuhara, Y. Fujii, K. Nishino, N. Isobe, M. Nakatake, L. Xian, A. Rubio, G. L. Lay, *2D Mater.* **2018**, *5*, 025002.

[24] C. Martella, G. Faraone, M. H. Alam, D. Taneja, L. Tao, G. Scavia, E. Bonera, C. Grazianetti, D. Akinwande, A. Molle, *Adv. Funct. Mater.* **2020**, *30*, 2004546.

[25] A. Molle, G. Faraone, A. Lamperti, D. Chiappe, E. Cinquanta, C. Martella, E. Bonera, E. Scalise, C. Grazianetti, *Faraday Discuss.* **2021**, *227*, 171.

[26] Y. Liu, N. Gao, J. Zhuang, C. Liu, J. Wang, W. Hao, S. X. Dou, J. Zhao, Y. Du, *J. Phys. Chem. Lett.* **2019**, *10*, 1558.

[27] W. Pang, K. Nishino, T. Ogikubo, M. Araidai, M. Nakatake, G. L. Lay, J. Yuhara, *Appl. Surf. Sci.* **2020**, *517*, 146224.

[28] D. Chiappe, C. Grazianetti, G. Tallarida, M. Fanciulli, A. Molle, *Adv. Mater.* **2012**, *24*, 5088.

[29] C. Grazianetti, D. Chiappe, E. Cinquanta, G. Tallarida, M. Fanciulli, A. Molle, *Appl. Surf. Sci.* **2014**, *291*, 109.

[30] P. Moras, T. O. Mentes, P. M. Sheverdyaeva, A. Locatelli, C. Carbone, *J. Phys.: Condens. Matter* **2014**, *26*, 185001.

[31] D.-A. Luh, C.-H. Wang, Y.-W. Yang, *Thin Solid Films* **2019**, *682*, 44.

[32] E. Cinquanta, E. Scalise, D. Chiappe, C. Grazianetti, B. van den Broek, M. Houssa, M. Fanciulli, A. Molle, *J. Phys. Chem. C* **2013**, *117*, 16719.

ADVANCED
SCIENCE NEWS

www.advancedsciencenews.com

ADVANCED
FUNCTIONAL
MATERIALS

www.afm-journal.de

[33] D. Solonenko, O. D. Gordan, G. L. Lay, D. R. T. Zahn, P. Vogt, *Beilstein J. Nanotechnol.* **2017**, *8*, 1357.

[34] P. Castrucci, F. Fabbri, T. Delise, M. Scarselli, M. Salvato, S. Pascale, R. Francini, I. Berbezier, C. Lechner, F. Jardali, H. Vach, M. De Crescenzi, *Nano Res.* **2018**, *11*, 5879.

[35] A. Molle, C. Grazianetti, D. Chiappe, E. Cinquanta, E. Cianci, G. Tallarida, M. Fanciulli, *Adv. Funct. Mater.* **2013**, *23*, 4340.

[36] X. Xu, J. Zhuang, Y. Du, H. Feng, N. Zhang, C. Liu, T. Lei, J. Wang, M. Spencer, T. Morishita, X. Wang, S. X. Dou, *Sci. Rep.* **2014**, *4*, 7543.

[37] Y. Du, J. Zhuang, J. Wang, Z. Li, H. Liu, J. Zhao, X. Xu, H. Feng, L. Chen, K. Wu, X. Wang, S. X. Dou, *Sci. Adv.* **2016**, *2*, e1600067.

[38] M. A. Stranick, A. Moskwa, *Surf. Sci. Spectra* **1993**, *2*, 50.

[39] R. I. Hegde, S. R. Sainkar, S. Badrinarayanan, A. P. B. Sinha, *J. Electron Spectrosc. Relat. Phenom.* **1981**, *24*, 19.

[40] C.-L. Lin, R. Arafune, K. Kawahara, M. Kanno, N. Tsukahara, E. Minamitani, Y. Kim, M. Kawai, N. Takagi, *Phys. Rev. Lett.* **2013**, *110*, 076801.

[41] D. Tsoutsou, E. Xenogiannopoulou, E. Golias, P. Tsipas, A. Dimoulas, *Appl. Phys. Lett.* **2013**, *103*, 231604.

[42] S. Cahangirov, M. Audiffred, P. Tang, A. Iacomino, W. Duan, G. Merino, A. Rubio, *Phys. Rev. B* **2013**, *88*, 035432.

[43] E. Cinquanta, G. Fratesi, S. dal Conte, C. Grazianetti, F. Scotognella, S. Stagira, C. Vozzi, G. Onida, A. Molle, *Phys. Rev. B* **2015**, *92*, 165427.

[44] P. M. Sheverdyaeva, S. K. Mahatha, P. Moras, L. Petaccia, G. Fratesi, G. Onida, C. Carbone, *ACS Nano* **2017**, *11*, 975.

[45] D. Chiappe, E. Scalise, E. Cinquanta, C. Grazianetti, B. van den Broek, M. Fanciulli, M. Houssa, A. Molle, *Adv. Mater.* **2014**, *26*, 2096.

[46] C. Grazianetti, S. De Rosa, C. Martella, P. Targa, D. Codegoni, P. Gori, O. Pulci, A. Molle, S. Lupi, *Nano Lett.* **2018**, *18*, 7124.

[47] M. E. Dávila, L. Xian, S. Cahangirov, A. Rubio, G. L. Lay, *New J. Phys.* **2014**, *16*, 095002.

[48] A. J. Mannix, X.-F. Zhou, B. Kiraly, J. D. Wood, D. Alducin, B. D. Myers, X. Liu, B. L. Fisher, U. Santiago, J. R. Guest, M. J. Yacaman, A. Ponce, A. R. Oganov, M. C. Hersam, N. P. Guisinger, *Science* **2015**, *350*, 1513.

[49] B. Feng, J. Zhang, Q. Zhong, W. Li, S. Li, H. Li, P. Cheng, S. Meng, L. Chen, K. Wu, *Nat. Chem.* **2016**, *8*, 563.

[50] Y. Shao, Z.-L. Liu, C. Cheng, X. Wu, H. Liu, C. Liu, J.-O. Wang, S.-Y. Zhu, Y.-Q. Wang, D.-X. Shi, K. Ibrahim, J.-T. Sun, Y.-L. Wang, H.-J. Gao, *Nano Lett.* **2018**, *18*, 2133.

[51] J. L. Zhang, S. Zhao, C. Han, Z. Wang, S. Zhong, S. Sun, R. Guo, X. Zhou, C. D. Gu, K. D. Yuan, Z. Li, W. Chen, *Nano Lett.* **2016**, *16*, 4903.

[52] X. Huang, J. Guan, Z. Lin, B. Liu, S. Xing, W. Wang, J. Guo, *Nano Lett.* **2017**, *17*, 4619.

[53] J. M. Soler, E. Artacho, J. D. Gale, A. García, J. Junquera, P. Ordejón, D. Sánchez-Portal, *J. Phys.: Condens. Matter* **2002**, *14*, 2745.

[54] A. García, N. Papior, A. Akhtar, E. Artacho, V. Blum, E. Bosoni, P. Brandimarte, M. Brandbyge, J. I. Cerdá, F. Corsetti, R. Cuadrado, V. Dikan, J. Ferrer, J. Gale, P. García-Fernández, V. M. García-Suárez, S. García, G. Huhs, S. Illera, R. Korytár, P. Koval, I. Lebedeva, L. Lin, P. López-Tarifa, S. G. Mayo, S. Mohr, P. Ordejón, A. Postnikov, Y. Pouillon, M. Pruneda, R. Robles, D. Sánchez-Portal, J. M. Soler, R. Ullah, V. W. Z. Yu, J. Junquera, *J. Chem. Phys.* **2020**, *152*, 204108.

[55] A. García, M. J. Verstraete, Y. Pouillon, J. Junquera, *Comput. Phys. Commun.* **2018**, *227*, 51.

[56] J. P. Perdew, K. Burke, M. Ernzerhof, *Phys. Rev. Lett.* **1996**, *77*, 3865.

[57] S. Grimme, *J. Comput. Chem.* **2006**, *27*, 1787.

[58] P. Giannozzi, S. Baroni, N. Bonini, M. Calandra, R. Car, C. Cavazzoni, D. Ceresoli, G. L. Chiarotti, M. Cococcioni, I. Dabo, A. Dal Corso, S. De Gironcoli, S. Fabris, G. Fratesi, R. Gebauer, U. Gerstmann, C. Gougoussis, A. Kokalj, M. Lazzeri, L. Martin-Samos, N. Marzari, F. Mauri, R. Mazzarello, S. Paolini, A. Pasquarello, L. Paulatto, C. Sbraccia, S. Scandolo, G. Sclauzero, A. P. Seitsonen, A. Smogunov, P. Umari, R. M. Wentzcovitch, *J. Phys.: Condens. Matter* **2009**, *21*, 395502.

2102797 (8 of 8)